

## Article

# Water Effect on the Electronic Properties and Lithium-Ion Conduction in a Defect-Engineered LiFePO<sub>4</sub> Electrode

Guoqing Wang <sup>1,2</sup>, Pengfei Xu <sup>1,\*</sup>, Halefom G. Desta <sup>2,3</sup>, Bayu Admasu Beshiwork <sup>3,4</sup> , Baihai Li <sup>2,4</sup>, Workneh Getachew Adam <sup>3</sup>  and Bin Lin <sup>2,4,\*</sup> 

<sup>1</sup> The 5th Electronics Research Institute, Ministry of Industry and Information Technology, Guangzhou 511370, China; wangguoqing@ceprei.biz

<sup>2</sup> School of Mechanical and Electrical Engineering, University of Electronic Science and Technology of China, Chengdu 611731, China; desta@uestc.edu.cn (H.G.D.); libaihai@uestc.edu.cn (B.L.)

<sup>3</sup> Department of Industrial Chemistry, College of Applied Science, Addis Ababa Science and Technology University, Addis Ababa P.O. Box 16417, Ethiopia; admasu.beshiwork@aastu.edu.et (B.A.B.); getachew.adam@aastu.edu.et (W.G.A.)

<sup>4</sup> Yangtze Delta Region Institute (Huzhou), University of Electronic Science and Technology of China, Huzhou 313001, China

\* Correspondence: xupf@ceprei.com (P.X.); bin@uestc.edu.cn (B.L.)

**Abstract:** Defect-engineering accelerates the conduction of lithium ions in the cathode materials of lithium-ion batteries. However, the effects of defect-engineering on ion conduction and its mechanisms in humid environments remain unclear in the academic discourse. Here, we report on the effect of vacancy defects on the electronic properties of and Li-ion diffusion in a LiFePO<sub>4</sub> material in humid environments. The research findings indicate that vacancy defects reduce the lattice constant and unit cell volume of LiFePO<sub>4</sub>. Additionally, the water molecules occupy the Li-ion vacancies, leading to an increase in the lattice constant of LiFePO<sub>4</sub>. The computational results of the electronic properties show that the introduction of water molecules induces a transition in LiFePO<sub>4</sub> from a semiconductor to a metallic behavior, with a transfer of 0.38 e of charge from the water molecules to LiFePO<sub>4</sub>. Additionally, the migration barrier for Li ions in the H<sub>2</sub>O + LiFePO<sub>4</sub> system is found to be 0.50 eV, representing an 11.1% increase compared to the pristine LiFePO<sub>4</sub> migration barrier. Our findings suggest that water molecules impede the migration of Li ions and provide important insights into the effect of defect-engineering on electronic properties and ion conduction under humid conditions.

**Keywords:** defect-engineering; ion conduction; humid environment; lithium-ion batteries



**Citation:** Wang, G.; Xu, P.; Desta, H.G.; Beshiwork, B.A.; Li, B.; Adam, W.G.; Lin, B. Water Effect on the Electronic Properties and Lithium-Ion Conduction in a Defect-Engineered LiFePO<sub>4</sub> Electrode. *Batteries* **2024**, *10*, 281. <https://doi.org/10.3390/batteries10080281>

Academic Editor: Carlos Ziebert

Received: 1 July 2024

Revised: 29 July 2024

Accepted: 3 August 2024

Published: 6 August 2024



**Copyright:** © 2024 by the authors. Licensee MDPI, Basel, Switzerland. This article is an open access article distributed under the terms and conditions of the Creative Commons Attribution (CC BY) license (<https://creativecommons.org/licenses/by/4.0/>).

## 1. Introduction

The current fossil fuel resources are insufficient to meet the demands of the rapid economic development, and the environmental pollution resulting from fossil fuel combustion is becoming increasingly severe [1–3]. Renewable energy contributes to the transformation of the global energy structure, and the consumption of renewable energy is a key constraint to its development [4,5]. Advanced energy materials and devices represented by lithium-ion batteries provide robust technological support for achieving high-efficiency energy storage and energy transition [6–9]. Lithium-ion batteries possess significant advantages such as high energy density, high power density, long cycle life, and environmental friendliness, which make them extensively utilized in energy storage and consumer electronics [10–12]. In recent years, there has been a significant growth trend in the demand for lithium-ion batteries, driven by the rapid development in fields such as electric vehicles and energy storage. LiFePO<sub>4</sub> stands out as a commercially successful cathode material for lithium-ion batteries due to its advantages of low production cost, high safety, and strong cycling stability [13–15]. It can effectively store energy, is not constrained by natural environments, and

mitigates the adverse impacts of intermittency, thereby improving the utilization efficiency of renewable energy [16–18]. The primary factors currently constraining the application of lithium-ion batteries are the cycling stability and safety of the LiFePO<sub>4</sub> material, and among them, humidity control stands out as a significant factor [19–22].

In the preparation process of LiFePO<sub>4</sub>, due to its small particle size and large specific surface area, problems such as powder aggregation and moisture absorption easily occur in humid environments. An uncontrolled moisture content in LiFePO<sub>4</sub> can lead to the decomposition of lithium salts in the electrolyte and hinder the film formation on the cathode material, ultimately resulting in the deterioration of the electrochemical properties of lithium-ion batteries [23,24]. Additionally, when LiFePO<sub>4</sub> is exposed to air for an extended period, moisture continuously infiltrates the material, leading to the formation of amorphous FePO<sub>4</sub>, ultimately resulting in aging and failure of LiFePO<sub>4</sub> [25]. Jarolimek et al. [26] research findings indicate that OH groups and H<sub>2</sub>O stably adsorb on the (010) surface of LiFePO<sub>4</sub>. After immersing LiFePO<sub>4</sub> in distilled water for 96 h, Xu et al. [27] observed that its initial discharge specific capacity and capacity after 20 cycles were 131.8 and 96 mAh/g, respectively. Compared to the values of 140 and 117 mAh/g for non-immersed samples, the cycling performance of LiFePO<sub>4</sub> deteriorated significantly after water immersion. Similarly, Jiang et al. [28] discussed the effect of moisture on LiFePO<sub>4</sub> under humid conditions. The results indicate that at temperatures ranging from 100 to 180 °C, H<sub>2</sub>O chemically reacts with LiFePO<sub>4</sub>, leading to a reduction in the lithium storage capacity of the material. Ahn et al. [29] investigated the impact of moisture on the electrochemical performance of LiFePO<sub>4</sub> (LFP)/Li<sub>7</sub>La<sub>3</sub>Zr<sub>2</sub>O<sub>12</sub> (LLZ) based solid-state batteries. The results revealed that exposure of the samples to humid air led to a decrease in the conductivity rate of Li ions at the grain boundary between LFP and LLZ.

Defect-engineering is regarded as a potent strategy for enhancing the electrochemical performance of batteries due to its capacity to facilitate the diffusion of Li ions within electrode materials. Wang et al. [30] reported the successful creation and introduction of a significant quantity of defects within the crystal lattice of a LiMn<sub>2</sub>O<sub>4</sub> material through defect-engineering, aiming to achieve enhanced Li-ion diffusion characteristics and rate performance in lithium-ion batteries. Lee et al. [31] combined first-principles calculations with scanning transmission electron microscopy to elucidate that Li-ion vacancies are confined within one-dimensional channels along the *b*-axis and are capable of migrating between adjacent Fe-Li sites. Amin et al. [32] discovered that the presence of lithium vacancies in LiFePO<sub>4</sub> crystals leads to a significant increase in Li-ion conductivity by more than three orders of magnitude after prolonged annealing at temperatures ranging from 300 °C to 500 °C. The activation energy for Li-ion diffusion decreased from 0.65 eV to 0.30 eV. In addition, Al doping introduces Li-ion vacancies into LiFePO<sub>4</sub>. The presence of Li-ion vacancies significantly enhances the diffusion rate of Li ions, resulting in LiFePO<sub>4</sub> exhibiting superior electrochemical performance at room temperature [33,34]. Aksyonov et al. [35] discovered that OH groups can infiltrate into the Li-ion vacancies of LiFePO<sub>4</sub>. Molecular dynamics simulation results indicate that OH groups can stably exist in LiFePO<sub>4</sub>. However, relatively little research has been conducted on how vacancy defects affect Li-ion conduction in LiFePO<sub>4</sub> under humid conditions.

Herein, we investigated the effect of defect-engineering on the conduction performance of electrons and Li ions in LiFePO<sub>4</sub> under humid conditions. Water molecule can enter Li-ion vacancies, leading to the expansion of the LiFePO<sub>4</sub> crystal structure. Density functional theory calculations demonstrated that water molecules lose electrons in Li-ion vacancy, causing LiFePO<sub>4</sub> to transition from a semiconductor to a metal. Water molecules enhance the electronic conductivity of LiFePO<sub>4</sub>. Furthermore, the introduction of H<sub>2</sub>O lowers the Li-ion migration barrier, thereby reducing the rate of ion conduction. Our study provides a physical mechanism for the effects of defect-engineering on Li-ion conduction behavior.

## 2. Methods

The VASP 5.4 (Vienna ab initio simulation package) software via DFT (density functional theory) was employed [36]. To describe the exchange–correlation effects, the PBE functional under the GGA was utilized [37]. The PAW method was employed to describe electronic wave functions [38,39]. The cut-off energy was 520 eV. The valence electron structures were selected as  $1s^1$  (H),  $2s^1$  (Li),  $2s^22p^4$  (O),  $3s^23p^3$  (P), and  $3d^74s^1$  (Fe). The convergence criteria for energy and atomic forces were set to  $10^{-6}$  eV and  $0.005$  eV/Å, respectively. To compensate for the underestimated correlation effect of the GGA method in the calculations for the strongly localized  $d$ -orbitals of the Fe element, the Hubbard correction (GGA + U) [40,41] was used to relax the ions and the cells, and the  $U_{\text{eff}}$  value for Fe atoms was taken as 4.3 eV [42]. The  $k$ -point of  $5 \times 3 \times 3$  was established. The DFT + D2 functional was employed [43]. The climbing image nudged elastic band (CI-NEB) method was used to calculate the migration paths and barriers of Li ions. The VESTA 4.6 software [44] was used to visualize the LiFePO<sub>4</sub> crystal structure.

## 3. Results and Discussion

### 3.1. Intrinsic Structure of LiFePO<sub>4</sub> and H<sub>2</sub>O + LiFePO<sub>4</sub>

The space group of LiFePO<sub>4</sub> is *Pnma*, and its configuration is in an orthorhombic olivine structure. In its unit cell, there are 4 Li, 4 Fe, 4 P, and 16 O atoms. Figure 1a depicts the  $1 \times 2 \times 1$  supercell of LiFePO<sub>4</sub>. The Li ions are situated within the octahedral interstices of the unit cell, forming a six-coordinated structure with the PO<sub>4</sub> groups. Fe<sup>2+</sup>, on the other hand, occupies the tetrahedral interstices of the unit cell, also forming a six-coordinated structure with the PO<sub>4</sub> groups. The PO<sub>4</sub> groups are connected to the Li ions and Fe<sup>2+</sup> through ionic bonds. The Li element and Fe element occupy the 4a and 4c Wyckoff positions in the octahedral sites, while the P element takes the 4c Wyckoff position in the tetrahedral site. In addition, due to the magnetic properties of iron, four magnetic configurations were considered and calculated for LiFePO<sub>4</sub>, i.e., ferromagnetic (FM), A-type antiferromagnetic (A-AFM), C-type antiferromagnetic (C-AFM), and G-type antiferromagnetic (G-AFM). The results indicated that the magnetic ground state of LiFePO<sub>4</sub> was C-AFM. After optimization, the structural parameters of LiFePO<sub>4</sub> were  $a = 4.727$  Å,  $b = 12.046$  Å,  $c = 10.282$  Å, and the volume was 585.47 Å<sup>3</sup>. When a Li vacancy was present in LiFePO<sub>4</sub>, its lattice constant and volume were reduced, and the cell volume decreased to 560.78 Å<sup>3</sup>. The data are listed in Table 1. The computational results in this study are consistent with the experimental measurements [45], indicating the reliability of the computational methods employed in this work.

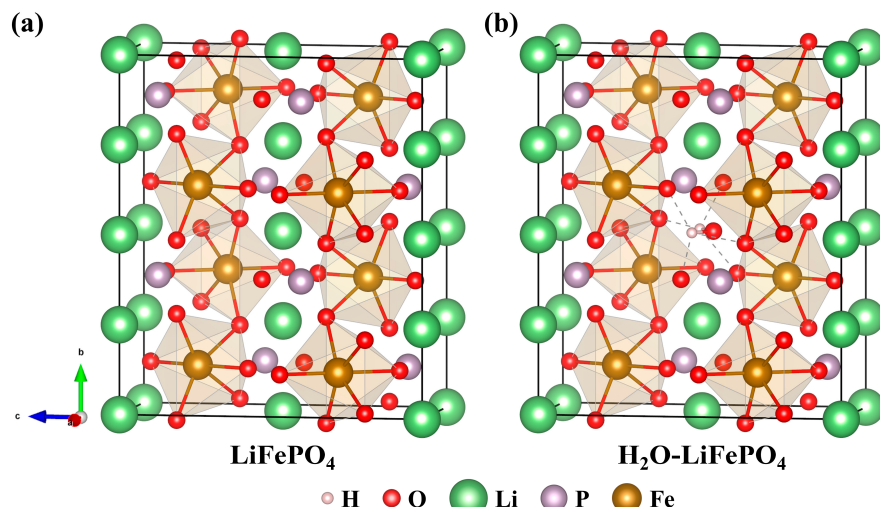


**Figure 1.** The structure of (a) pristine LiFePO<sub>4</sub> and (b) H<sub>2</sub>O + LiFePO<sub>4</sub>. White, red, green, purple, and brown balls represent H, O, Li, P, and Fe elements, respectively.

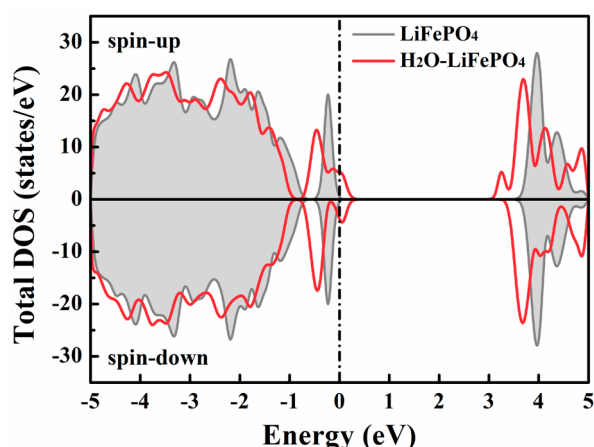
**Table 1.** Lattice constant ( $\text{\AA}$ ) and volume ( $\text{\AA}^3$ ) of  $\text{LiFePO}_4$ ,  $\text{Li}_{0.875}\text{FePO}_4$ , and  $\text{H}_2\text{O} + \text{LiFePO}_4$ .

Case	<i>a</i>	<i>b</i>	<i>c</i>	<i>V</i>	Ref.
$\text{LiFePO}_4$	4.727	12.046	10.282	585.47	this work
$\text{Li}_{0.875}\text{FePO}_4$	4.680	11.861	10.103	560.78	this work
$\text{H}_2\text{O} + \text{LiFePO}_4$	4.756	12.122	10.346	596.47	this work
$\text{LiFePO}_4$	4.692	12.022	10.332	582.80	[45]

In a humid environment, water molecules infiltrate the  $\text{LiFePO}_4$  material. During the discharge process of  $\text{LiFePO}_4$ , a significant number of Li vacancies are generated; hence, there is a high probability that the water molecules will occupy these Li vacancies. Here, we discuss the structural changes of  $\text{LiFePO}_4$  after a water molecule ( $\text{H}_2\text{O}$ ) occupies a Li vacancy, as shown in Figure 1b. After structural optimization, the lattice constants were  $a = 4.756 \text{ \AA}$ ,  $b = 12.122 \text{ \AA}$ ,  $c = 10.346 \text{ \AA}$ , and the unit cell volume was  $596.47 \text{ \AA}^3$ . In this system, there were 2 H, 7 Li, 8 Fe, 8 P, and 33 O atoms, totaling 58 atoms. In comparison to the  $\text{LiFePO}_4$ , the addition of  $\text{H}_2\text{O}$  resulted in an increase in both lattice constants and unit cell volume, and the water molecule concentration was 12.5%. This is attributed to the larger radius of the water molecules compared to the Li ions they replaced, which readily induced lattice expansion upon incorporation into the lattice. It is commonly believed that an increase in the unit cell volume of a material can provide more space for the extraction and insertion of Li ions, thereby enhancing the rate of Li-ion conduction within the electrode [46–48].

### 3.2. Electronic Properties of $\text{LiFePO}_4$ and $\text{H}_2\text{O} + \text{LiFePO}_4$

The total density of states (DOS) is used to describe the number of electronic states within a specified energy range per unit energy or volume. Figure 2 shows the total DOS of  $\text{LiFePO}_4$  (gray shadow) and  $\text{H}_2\text{O} + \text{LiFePO}_4$  (red curve).  $\text{LiFePO}_4$  is a semiconductor and possesses a band gap of approximately 3.5 eV. Detailed band-gap data are provided in the energy band structure of  $\text{LiFePO}_4$  below. As for  $\text{Fe}^{2+}$ , six electrons occupy the spin-up states of the  $t_{2g}$  and  $e_g$  orbitals in the  $3d$  subshell, along with one spin-down state of the  $t_{2g}$  orbital, while the spin-down states of the  $e_g$  orbitals remain unoccupied. Moreover, due to the C-AFM ground state of  $\text{LiFePO}_4$ , the spin-up and spin-down DOS are completely symmetric, and the total magnetic moment of the entire system is  $0 \mu_B$ . For the  $\text{H}_2\text{O} + \text{LiFePO}_4$  system, from the red curve in Figure 2, it is evident that there are electronic states crossing the Fermi level, indicating that the addition of  $\text{H}_2\text{O}$  resulted in the presence of free electrons in  $\text{LiFePO}_4$ . The system exhibited an external magnetic moment of  $1 \mu_B$ . Therefore, upon the occupation of the Li-ion vacancies by  $\text{H}_2\text{O}$ , the contribution of the free electrons caused  $\text{LiFePO}_4$  to undergo a transition from a semiconductor to a metal, thereby enhancing the intrinsic electronic conductivity of  $\text{LiFePO}_4$  to a certain extent.

**Figure 2.** Total DOS of  $\text{LiFePO}_4$  (gray shadow) and  $\text{H}_2\text{O} + \text{LiFePO}_4$  (red curve).

The electronic bands exhibited diverse energy structures due to differences in the orbitals occupied within atoms. A small band gap facilitates electron transitions, leading to better conductivity of the material. Conversely, a large band gap makes electron transitions more difficult, resulting in poorer conductivity. The band gap for pristine LiFePO<sub>4</sub> was calculated to be 3.542 eV, demonstrating strong agreement with theoretical and experimental studies [49,50], as shown in Figure 3a. In the band structure, the blue and red lines represent spin-up and spin-down states, respectively. In addition, the valence band maximum is located at the M-point, and the conduction band minimum is situated at the G-point, thus categorizing LiFePO<sub>4</sub> as an indirect band-gap semiconductor material. For pristine LiFePO<sub>4</sub>, due to its ground state magnetic configuration being C-AFM, the spin-up state and spin-down state overlap in the electronic band structure. Furthermore, the C-AFM ground state can induce coupling effects between local electronic states and magnetic states, resulting in changes in the local density of the states, which in turn affects the electronic structure and conductivity.

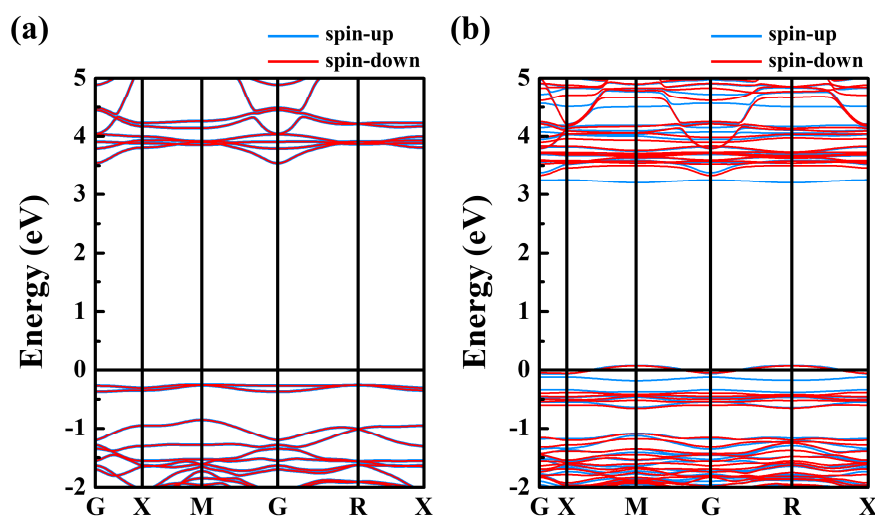


**Figure 3.** Electronic band structures of (a) LiFePO<sub>4</sub> and (b) H<sub>2</sub>O + LiFePO<sub>4</sub>. The blue and red lines represent spin-up and spin-down states, respectively. The Fermi energy was set to zero.

In the H<sub>2</sub>O + LiFePO<sub>4</sub> system, we could clearly observe that the introduction of water molecules caused a splitting of the system's band structure. The spin-up states and spin-down states did not overlap, as shown in Figure 3b. In this case, the presence of a band crossing the Fermi level directly demonstrated the transition of LiFePO<sub>4</sub> from a semiconductor to a metallic behavior upon the addition of water molecule. Furthermore, the presence of water molecules led to a denser band structure throughout the H<sub>2</sub>O + LiFePO<sub>4</sub> system, with an increased number of bands due to the introduction of the water molecule. This facilitated the electron transition process from the valence band to the conduction band, making it easier for electrons to move across this transition. After occupying the Li-ion vacancies, the water molecules increased the electronic conductivity of LiFePO<sub>4</sub>, thereby enhancing the electrical performance of the electrode material to some extent in a humid environment.

### 3.3. Charge Properties of LiFePO<sub>4</sub> and H<sub>2</sub>O + LiFePO<sub>4</sub>

Bader charge analysis [51] is a quantitative method for computing the charge distribution among individual elements within a material. This method is commonly applied to analyze material structures, bonding characteristics, and interactions between different elements or atoms. According to Bader charge analysis, in pristine LiFePO<sub>4</sub>, each Li, Fe, and P atom lost 0.87 e, 1.43 e, and 3.62 e, respectively, and each O atom gained 1.48 e. In the H<sub>2</sub>O + LiFePO<sub>4</sub> system, each Li, Fe, and P atom lost 0.86 e, 1.44 e, and 3.60 e, respectively, and each O atom gained 1.46 e. As a whole, H<sub>2</sub>O lost 0.38 e. At this point, LiFePO<sub>4</sub> gained

0.38  $e$  from  $\text{H}_2\text{O}$ . The average charge gains and loss data are listed for each element in Table 2.

**Table 2.** Average charge gains and losses ( $e$ ) for each element in  $\text{LiFePO}_4$  and  $\text{H}_2\text{O} + \text{LiFePO}_4$ , where a negative value indicates a loss of charge, and a positive value a gain of charge.

Case	Li	Fe	P	O	$\Sigma_{\text{LiFePO}_4}$	$\Sigma_{\text{H}_2\text{O}}$
$\text{LiFePO}_4$	-0.87	-1.43	-3.62	+1.48	0.00	—
$\text{H}_2\text{O} + \text{LiFePO}_4$	-0.86	-1.44	-3.60	+1.46	+0.38	-0.38

The charge density difference map is employed to analyze the variations in electron density between two systems, facilitating a detailed investigation of bonding characteristics, inter-system interactions, charge transfer, and other physico-chemical phenomena. Here, we computed the charge density difference between  $\text{H}_2\text{O}$  and  $\text{LiFePO}_4$  within the system, as shown in Figure 4, according to the following formula:

$$\Delta\rho(z) = \int \rho_{\text{H}_2\text{O}+\text{LiFePO}_4}(x, y, z) dx dy dz - \int \rho_{\text{H}_2\text{O}}(x, y, z) dx dy dz - \int \rho_{\text{LiFePO}_4}(x, y, z) dx dy dz$$

where  $\rho_{\text{H}_2\text{O}+\text{LiFePO}_4}(x, y, z)$ ,  $\rho_{\text{H}_2\text{O}}(x, y, z)$ , and  $\rho_{\text{LiFePO}_4}(x, y, z)$  are the charge densities of  $\text{H}_2\text{O} + \text{LiFePO}_4$  system, water molecule, and  $\text{LiFePO}_4$  at the  $(x, y, z)$  point, respectively. In Figure 4, the blue region indicates electron depletion, while the yellow region signifies electron accumulation. We can observe that a water molecule is located in a Li-ion vacancy, surrounded by the blue region, indicating a loss of charge by the water molecule and its transfer into  $\text{LiFePO}_4$ . The charge density difference not only further confirmed the transfer of charge from water molecules to  $\text{LiFePO}_4$ , but also provided us with visual evidence of their interaction. This computational result is consistent with the conclusions obtained from Bader charge analysis, demonstrating the occurrence of charge transfer between  $\text{H}_2\text{O}$  and  $\text{LiFePO}_4$  in a humid environment.

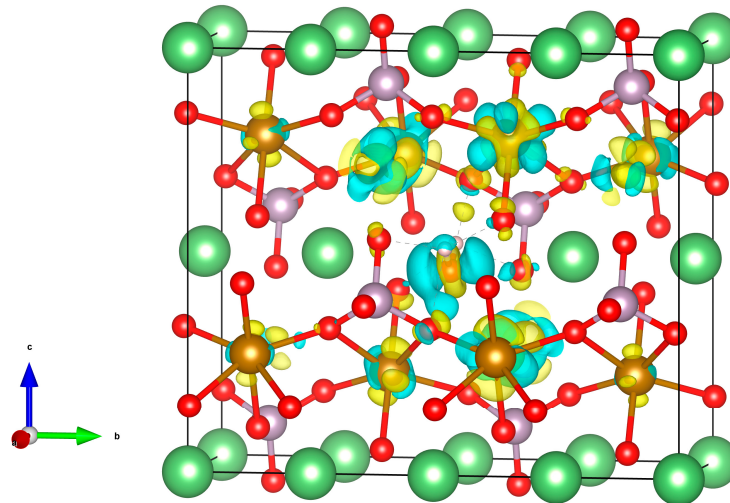


**Figure 4.** The charge density difference for  $\text{H}_2\text{O} + \text{LiFePO}_4$ . The blue region indicates electron depletion, and the yellow region means electron accumulation. The isosurface value was  $0.0075 \text{ e/Bohr}^3$ .

Furthermore, we conducted a detailed analysis of electron localization function (ELF) maps for pristine  $\text{LiFePO}_4$  and the  $\text{H}_2\text{O} + \text{LiFePO}_4$  system, as shown in Figure 5. The ELF method is used to study the electronic structure and bonding states of materials [52,53]. This method is employed to characterize the probability of finding an electron with a specific spin in a particular region, thereby delineating the degree of electron localization around atoms. In Figure 5a, it can be observed that there are red regions clustering around the O atoms, indicating that the electrons are predominantly localized around the O element on

the (010) crystal face. After the water molecules occupy the Li-ion vacancies, the color of the red regions around the O atoms becomes lighter, indicating a decrease in the localized charge density around the O element, as shown in Figure 5b. This is consistent with the data from Bader charge analysis. When LiFePO<sub>4</sub> was in a humid environment, the average charge on the O atoms decreased from 1.48 e to 1.46 e, denoting a reduction in the electrons gained by the O element.

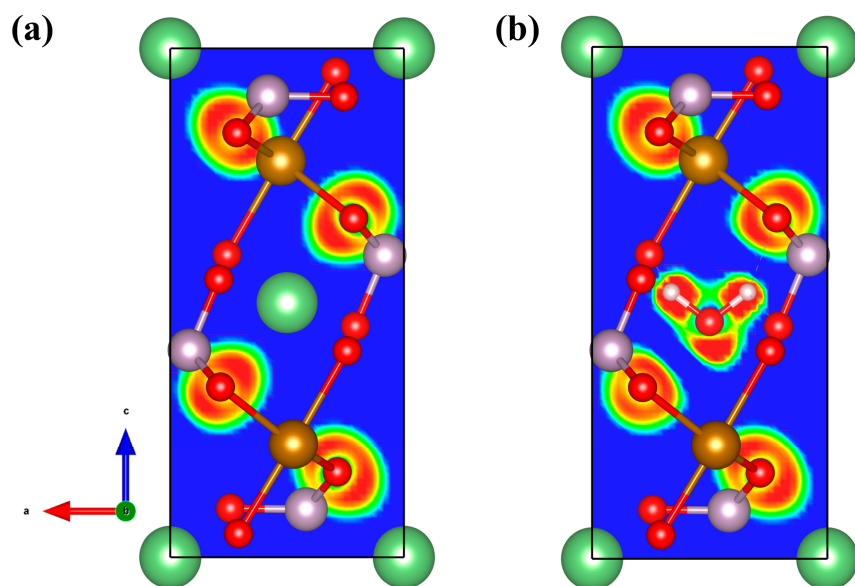


**Figure 5.** The electron localization function map on the (010) crystal face of (a) pristine LiFePO<sub>4</sub> and (b) H<sub>2</sub>O + LiFePO<sub>4</sub>.

### 3.4. Migration Properties of the Li Ion in LiFePO<sub>4</sub> and H<sub>2</sub>O + LiFePO<sub>4</sub>

The migration barriers of Li ions within electrode materials have a significantly impact on the rate performance of lithium-ion batteries and serve as a crucial factor determining their overall performance. In LiFePO<sub>4</sub>, the migration path of Li ions is constrained within one-dimensional channels along the *b*-direction [54,55]. Nishimura et al. [56] observed the one-dimensional characteristics of Li-ion diffusion channels within the LiFePO<sub>4</sub> material experimentally. Based on structural symmetry, it is evident that there was only one migration pathway for Li ions, with a migration barrier of ~0.45 eV. In addition, we analyzed the migration properties of Li ions in H<sub>2</sub>O + LiFePO<sub>4</sub>. The computational results indicated that the migration barrier for the Li ions increased to 0.50 eV, as shown in Figure 6. Compared to the pristine LiFePO<sub>4</sub>, the migration barrier for Li ions in H<sub>2</sub>O + LiFePO<sub>4</sub> increased by approximately 11.1%. Hence, the addition of H<sub>2</sub>O increased the migration barrier for Li ions, hindering their diffusion and consequently reducing their migration rate. After a water molecule occupies a Li-ion vacancy, it can obstruct the one-dimensional diffusion channels of the Li ion, thereby hindering ion migration. Ultimately, this leads to a decline in the rate performance of LiFePO<sub>4</sub>. In summary, moisture has a significant impact on the migration of Li ions, and the introduction of H<sub>2</sub>O will severely impede the migration of Li ions. Therefore, during the preparation and use of actual electrode materials, it is crucial to strictly control the introduction of moisture.

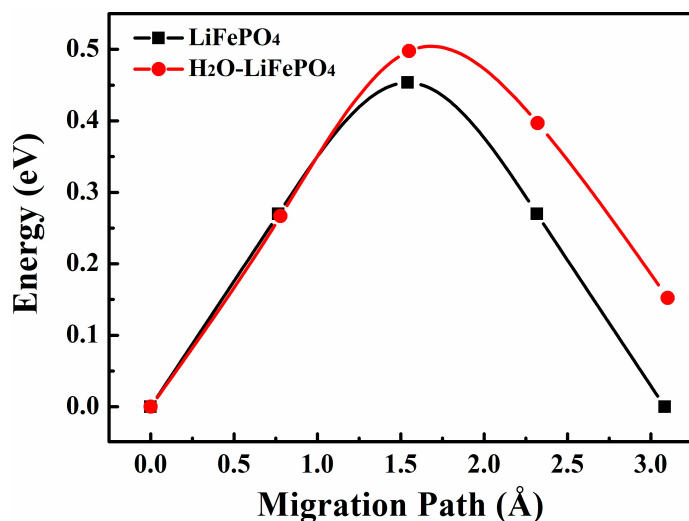


**Figure 6.** The migration barriers of Li ions in pristine LiFePO<sub>4</sub> (black curve) and H<sub>2</sub>O + LiFePO<sub>4</sub> (red curve).

#### 4. Conclusions

In short, this work systematically investigated the influence of a humid environment on the performance of LiFePO<sub>4</sub> as a lithium-ion battery electrode material, using the first-principles methods. Magnetic studies revealed that the ground state of pristine LiFePO<sub>4</sub> is C-type antiferromagnetism. LiFePO<sub>4</sub> is a semiconductor with a band gap of 3.542 eV. The stable framework structure of FePO<sub>4</sub> allows water molecules to enter and occupy Li vacancies in humid environments. When a water molecule (H<sub>2</sub>O) occupies a Li vacancy, the lattice constants and volume of the system increase. In the H<sub>2</sub>O + LiFePO<sub>4</sub> system, the charge of 0.38  $e$  lost by H<sub>2</sub>O was transferred to LiFePO<sub>4</sub>, and the charge density difference and electron localization function both confirmed this result. The total DOS and band structure indicated that the introduction of water molecules enhanced the overall electronic conductivity of the H<sub>2</sub>O + LiFePO<sub>4</sub> system. At this point, the H<sub>2</sub>O + LiFePO<sub>4</sub> system exhibited an external magnetic moment of 1  $\mu_B$ . In addition, the migration barrier for Li ions in pristine LiFePO<sub>4</sub> was 0.45 eV. In the H<sub>2</sub>O + LiFePO<sub>4</sub> system, the migration barrier for Li ions increased to 0.50 eV, representing an increase of 11.1%. This severely hindered the migration performance of Li ions, resulting in a decline in the performance of LiFePO<sub>4</sub> during charging and discharge processes. Our study revealed the influence of water molecules on the performance of lithium-ion battery electrode materials in a humid environment. Overall, the above research results revealed the effect of a humid environment on the performance of LiFePO<sub>4</sub> materials, providing a theoretical basis for subsequent experimental investigations into the coupled interaction between water molecules and LiFePO<sub>4</sub>.

**Author Contributions:** G.W.: writing—original draft, visualization, data curation, formal analysis, funding acquisition. P.X.: writing—review and editing, methodology, validation. H.G.D.: writing—review and editing. B.A.B.: writing—review and editing. B.L. (Baihai Li): writing—review and editing. W.G.A.: writing—review and editing, Conceptualization. B.L. (Bin Lin): writing—review and editing, conceptualization, supervision. All authors have read and agreed to the published version of the manuscript.

**Funding:** This work was supported by the Key-Area Research and Development Program of Guangdong Province under Grant No. 2023B0909060004.

**Data Availability Statement:** Data will be made available on request.

**Conflicts of Interest:** The authors declare no conflicts of interest.

## References

- Shindell, D.; Smith, C.J. Climate and air-quality benefits of a realistic phase-out of fossil fuels. *Nature* **2019**, *573*, 408–411. [[CrossRef](#)] [[PubMed](#)]
- Zhu, S.Y.; Yuan, Y.F.; Du, P.F.; Zhu, M.; Chen, Y.B.; Guo, S.Y.  $\alpha$ -MnS nanoparticles in-situ anchored in 3D macroporous honeycomb carbon as high-performance anode for Li-ion batteries. *Appl. Surf. Sci.* **2023**, *616*, 156619. [[CrossRef](#)]
- Yasin, G.; Arif, M.; Mehtab, T.; Lu, X.; Yu, D.; Muhammad, N.; Nazir, M.T.; Song, H. Understanding and suppression strategies toward stable Li metal anode for safe lithium batteries. *Energy Storage Mater.* **2020**, *25*, 644–678. [[CrossRef](#)]
- Jansen, A.N.; Kahaian, A.J.; Kepler, K.D.; Nelson, P.A.; Amine, K.; Dees, D.W.; Vissers, D.R.; Thackeray, M.M. Development of a high-power lithium-ion battery. *J. Power Sources* **1999**, *81*, 902–905. [[CrossRef](#)]
- Smith, K.; Wang, C.Y. Power and thermal characterization of a lithium-ion battery pack for hybrid-electric vehicles. *J. Power Sources* **2006**, *160*, 662–673. [[CrossRef](#)]
- Schmuck, R.; Wagner, R.; Horpel, G.; Placke, T.; Winter, M. Performance and cost of materials for lithium-based rechargeable automotive batteries. *Nat. Energy* **2018**, *3*, 267–278. [[CrossRef](#)]
- Ahuis, M.; Doose, S.; Vogt, D.; Michalowski, P.; Zellmer, S.; Kwade, A. Recycling of solid-state batteries. *Nat. Energy* **2024**, *9*, 373–385. [[CrossRef](#)]
- Dai, Q.; Kelly, J.C.; Gaines, L.; Wang, M. Life cycle analysis of lithium-ion batteries for automotive applications. *Batteries* **2019**, *5*, 48. [[CrossRef](#)]
- Yuan, Y.; Xu, L.; Wang, J.; Yan, W.; Huang, X.; Guo, S. 1D-in-1D multi-core CoSe<sub>2</sub> nanowires@porous carbon fiber for high-rate and long-life sodium storage. *J. Energy Storage* **2024**, *93*, 112328. [[CrossRef](#)]
- Armand, M.; Tarascon, J.M. Building better batteries. *Nature* **2008**, *451*, 652–657. [[CrossRef](#)]
- Lu, Z.; Wang, Q.; Xu, F.; Fan, M.; Peng, C.; Yan, S. Double-layer SOC and SOH equalization scheme for LiFePO<sub>4</sub> battery energy storage system using MAS blackboard system. *Energies* **2023**, *16*, 5460. [[CrossRef](#)]
- Yuan, Y.F.; Xi, J.C.; Zhang, T.; Wang, B.X.; Guo, S.Y.; Huang, Y.Z.; Yang, Q.H. Co-Fe Prussian blue analogue ultrafine nanocrystal cubes grown in-situ in honeycomb carbon as high-performance anode for lithium-ion batteries. *Appl. Surf. Sci.* **2023**, *640*, 158456. [[CrossRef](#)]
- Padhi, A.K.; Nanjundaswamy, K.S.; Goodenough, J.B. Phospho-olivines as positive-electrode materials for rechargeable lithium batteries. *J. Electrochem. Soc.* **1997**, *144*, 1188. [[CrossRef](#)]
- Pan, H.; Wang, L.; Shi, Y.; Sheng, C.; Yang, S.; He, P.; Zhou, H. A solid-state lithium-ion battery with micron-sized silicon anode operating free from external pressure. *Nat. Commun.* **2024**, *15*, 2263. [[CrossRef](#)] [[PubMed](#)]
- Huang, Z.Y.; Yuan, Y.F.; Lin, Z.C.; Lin, J.J.; Li, S.B.; Guo, S.Y.; Huang, Y.Z.; Yan, W.W. Fluffy ultrathin WO<sub>3</sub> nanoneedle clusters in-situ grown in mesoporous hollow carbon nanospheres as advanced anode for lithium-ion batteries. *J. Alloys Compd.* **2023**, *969*, 172458. [[CrossRef](#)]
- Jiang, X.; Xin, Y.; He, B.; Zhang, F.; Tian, H. Effect of heteroatom doping on electrochemical properties of olivine LiFePO<sub>4</sub> cathodes for high-performance lithium-ion batteries. *Materials* **2024**, *17*, 1299. [[CrossRef](#)] [[PubMed](#)]
- Zeng, Z.; Lei, H.; Li, J.; Yuan, Z.; Wang, B.; Zhao, W.; Yang, Y.; Ge, P. Designing functional Li<sub>2</sub>CuO<sub>2</sub>-coated separators from Cu foil towards spent LiFePO<sub>4</sub> cathode regeneration. *Chem. Commun.* **2024**, *60*, 3059–3062. [[CrossRef](#)] [[PubMed](#)]
- Yasin, G.; Arif, M.; Ma, J.; Ibraheem, S.; Yu, D.; Zhang, L.; Liu, D.; Dai, L. Self-templating synthesis of heteroatom-doped large-scalable carbon anodes for high-performance lithium-ion batteries. *Inorg. Chem. Front.* **2022**, *9*, 1058–1069. [[CrossRef](#)]
- Liu, Y.; Xue, J.S.; Zheng, T.; Dahn, J.R. Mechanism of lithium insertion in hard carbons prepared by pyrolysis of epoxy resins. *Carbon* **1996**, *34*, 193–200. [[CrossRef](#)]
- Benkreira, H.; Shibata, Y.; Ito, K. Thinnest uniform liquid films formed at the highest speeds with reverse roll coating. *AIChE J.* **2013**, *59*, 3083–3091. [[CrossRef](#)]
- Shen, C.; Wan, L. A design methodology for lithium-ion battery management system and its application to an autonomous underwater vehicle. *Adv. Mater. Res.* **2012**, *383*, 7175–7182. [[CrossRef](#)]
- Miao, B.; Lv, J.; Wang, Q.; Zhu, G.; Guo, C.; An, G.; Ou, J. The suppression effect of water mist released at different stages on lithium-ion battery flame temperature, heat release, and heat radiation. *Batteries* **2024**, *10*, 232. [[CrossRef](#)]
- Liu, G.Q.; Wen, L.; Liu, Y.M. Spinel LiNi<sub>0.5</sub>Mn<sub>1.5</sub>O<sub>4</sub> and its derivatives as cathodes for high-voltage Li-ion batteries. *J. Solid State Electrochem.* **2010**, *14*, 2191–2202. [[CrossRef](#)]
- Delaporte, N.; Trudeau, M.L.; Belanger, D.; Zaghib, K. Protection of LiFePO<sub>4</sub> against Moisture. *Materials* **2020**, *13*, 942. [[CrossRef](#)] [[PubMed](#)]
- Cuisinier, M.; Martin, J.-F.; Dupré, N.; Kanno, R.; Guyomard, D. Elucidating the LiFePO<sub>4</sub> air aging mechanism to predict its electrochemical performance. *J. Mater. Chem.* **2011**, *21*, 18575–18583. [[CrossRef](#)]
- Jarolimek, K.; Risko, C. Modification of the LiFePO<sub>4</sub> (010) surface due to exposure to atmospheric gases. *ACS Appl. Mater. Interfaces* **2021**, *13*, 29034–29040. [[CrossRef](#)] [[PubMed](#)]
- Xu, D.; Gao, S.; Zheng, W.; Cheng, L.; Feng, L.; Shui, M.; Shu, J. Properties of LIB cathode material LiFePO<sub>4</sub> after extreme water soaking conditions. *Chin. Battery Ind.* **2012**, *17*, 161–164.
- Xu, H.; Jiang, S. Influence of moisture on electrical properties of lithium iron phosphate. *Chin. J. Power Sources* **2019**, *43*, 1284–1286.
- Ahn, C.-W.; Choi, J.-J.; Ryu, J.; Hahn, B.-D.; Kim, J.-W.; Yoon, W.-H.; Choi, J.-H.; Lee, J.-S.; Park, D.-S. Electrochemical properties of Li<sub>7</sub>La<sub>3</sub>Zr<sub>2</sub>O<sub>12</sub>-based solid state battery. *J. Power Sources* **2014**, *272*, 554–558. [[CrossRef](#)]

30. Wang, R.; Chen, X.; Huang, Z.; Yang, J.; Liu, F.; Chu, M.; Liu, T.; Wang, C.; Zhu, W.; Li, S.; et al. Twin boundary defect engineering improves lithium-ion diffusion for fast-charging spinel cathode materials. *Nat. Commun.* **2021**, *12*, 3085. [[CrossRef](#)]
31. Lee, J.; Zhou, W.; Idrobo, J.C.; Pennycook, S.J.; Pantelides, S.T. Vacancy-driven anisotropic defect distribution in the battery-cathode material LiFePO<sub>4</sub>. *Phys. Rev. Lett.* **2011**, *107*, 085507. [[CrossRef](#)]
32. Amin, R.; Maier, J. Effect of annealing on transport properties of LiFePO<sub>4</sub>: Towards a defect chemical model. *Solid State Ion.* **2008**, *178*, 1831–1836. [[CrossRef](#)]
33. Amin, R.; Lin, C.; Maier, J. Aluminium-doped LiFePO<sub>4</sub> single crystals. *Phys. Chem. Chem. Phys.* **2008**, *10*, 3519–3523. [[CrossRef](#)]
34. Amin, R.; Lin, C.; Maier, J. Aluminium-doped LiFePO<sub>4</sub> single crystals. *Phys. Chem. Chem. Phys.* **2008**, *10*, 3524–3529. [[CrossRef](#)]
35. Aksyonov, D.A.; Varlamova, I.; Trussov, I.A.; Savina, A.A.; Senyshyn, A.; Stevenson, K.J.; Abakumov, A.M.; Zhugayevych, A.; Fedotov, S.S. Hydroxyl defects in LiFePO<sub>4</sub> cathode material: DFT+U and an experimental study. *Inorg. Chem.* **2021**, *60*, 5497–5506. [[CrossRef](#)]
36. Kresse, G.; Hafner, J. *Ab initio* molecular-dynamics simulation of the liquid-metal–amorphous-semiconductor transition in germanium. *Phys. Rev. B* **1994**, *49*, 14251–14269. [[CrossRef](#)]
37. Perdew, J.P.; Burke, K.; Ernzerhof, M. Generalized gradient approximation made simple. *Phys. Rev. Lett.* **1996**, *77*, 3865–3868. [[CrossRef](#)]
38. Kresse, G.; Joubert, D. From ultrasoft pseudopotentials to the projector augmented-wave method. *Phys. Rev. B* **1999**, *59*, 1758–1775. [[CrossRef](#)]
39. Blöchl, P.E. Projector augmented-wave method. *Phys. Rev. B* **1994**, *50*, 17953–17979. [[CrossRef](#)]
40. Anisimov, V.I.; Solovyev, I.V.; Korotin, M.A.; Czyżk, M.T.; Sawatzky, G.A. Density-functional theory and NiO photoemission spectra. *Phys. Rev. B* **1993**, *48*, 16929–16934. [[CrossRef](#)]
41. Lichtenstein, A. First-principles calculations of electronic structure and spectra of strongly correlated systems: The LDA+U method. *J. Phys. Condens. Matter* **1995**, *9*, 767–808.
42. Zhou, F.; Kang, K.; Maxisch, T.; Ceder, G.; Morgan, D. The electronic structure and band gap of LiFePO<sub>4</sub> and LiMnPO<sub>4</sub>. *Solid State Commun.* **2004**, *132*, 181–186. [[CrossRef](#)]
43. Grimme, S.; Antony, J.; Ehrlich, S.; Krieg, H. A consistent and accurate ab initio parametrization of density functional dispersion correction (DFT-D) for the 94 elements H–Pu. *J. Chem. Phys.* **2010**, *132*, 154104. [[CrossRef](#)]
44. Momma, K.; Izumi, F. VESTA: A three-dimensional visualization system for electronic and structural analysis. *J. Appl. Crystallogr.* **2008**, *41*, 653–658. [[CrossRef](#)]
45. Streltsov, V.A.; Belokoneva, E.L.; Tsirelson, V.G.; Hansen, N.K. Multipole analysis of the electron density in triphylite, LiFePO<sub>4</sub>, using X-ray diffraction data. *Acta Crystallogr. Sect. B* **1993**, *49*, 147–153. [[CrossRef](#)]
46. Liu, H.; Ren, Z.; Zhang, X.; Hu, J.; Gao, M.; Pan, H.; Liu, Y. Incorporation of ammonia borane groups in the lithium borohydride structure enables ultrafast lithium ion conductivity at room temperature for solid-state batteries. *Chem. Mater.* **2020**, *32*, 671–678. [[CrossRef](#)]
47. Zhang, Y.; Chen, Z.; Shi, X.; Meng, C.; Das, P.; Zheng, S.; Pan, F.; Wu, Z.-S. Regulation of 3d-transition metal interlayered disorder by appropriate lithium depletion for Li-rich layered oxide with remarkably enhanced initial coulombic efficiency and stability. *Adv. Energy Mater.* **2023**, *13*, 2203045. [[CrossRef](#)]
48. Yuan, L.-X.; Wang, Z.-H.; Zhang, W.-X.; Hu, X.-L.; Chen, J.-T.; Huang, Y.-H.; Goodenough, J.B. Development and challenges of LiFePO<sub>4</sub> cathode material for lithium-ion batteries. *Energy Environ. Sci.* **2011**, *4*, 269–284. [[CrossRef](#)]
49. Karimzadeh, S.; Safaei, B.; Huang, W.; Jen, T.-C. Theoretical investigation on niobium doped LiFePO<sub>4</sub> cathode material for high performance lithium-ion batteries. *J. Energy Storage* **2023**, *67*, 107572. [[CrossRef](#)]
50. Molenda, J.; Kulka, A.; Milewska, A.; Zajac, W.; Świerczek, K. Structural, transport and electrochemical properties of LiFePO<sub>4</sub> substituted in lithium and iron sublattices (Al, Zr, W, Mn, Co and Ni). *Materials* **2013**, *6*, 1656–1687. [[CrossRef](#)]
51. Henkelman, G.; Arnaldsson, A.; Jónsson, H. A fast and robust algorithm for Bader decomposition of charge density. *Comput. Mater. Sci.* **2006**, *36*, 354–360. [[CrossRef](#)]
52. Gibbs, G.V.; Cox, D.F.; Ross, N.L.; Crawford, T.D.; Downs, R.T.; Burt, J.B. Comparison of the electron localization function and deformation electron density maps for selected earth materials. *J. Phys. Chem. A* **2005**, *109*, 10022–10027. [[CrossRef](#)]
53. Gibbs, G.V.; Cox, D.F.; Ross, N.L.; Crawford, T.D.; Burt, J.B.; Rosso, K.M. A mapping of the electron localization function for earth materials. *Phys. Chem. Miner.* **2005**, *32*, 208–221. [[CrossRef](#)]
54. Morgan, D.; Van der Ven, A.; Ceder, G. Li conductivity in Li<sub>x</sub>MPO<sub>4</sub> (M = Mn, Fe, Co, Ni) olivine materials. *Electrochim. Solid-State Lett.* **2003**, *7*, A30. [[CrossRef](#)]
55. Ouyang, C.; Shi, S.; Wang, Z.; Huang, X.; Chen, L. First-principles study of Li ion diffusion in LiFePO<sub>4</sub>. *Phys. Rev. B* **2004**, *69*, 104303. [[CrossRef](#)]
56. Nishimura, S.-I.; Kobayashi, G.; Ohoyama, K.; Kanno, R.; Yashima, M.; Yamada, A. Experimental visualization of lithium diffusion in Li<sub>x</sub>FePO<sub>4</sub>. *Nat. Mater.* **2008**, *7*, 707–711. [[CrossRef](#)]

**Disclaimer/Publisher's Note:** The statements, opinions and data contained in all publications are solely those of the individual author(s) and contributor(s) and not of MDPI and/or the editor(s). MDPI and/or the editor(s) disclaim responsibility for any injury to people or property resulting from any ideas, methods, instructions or products referred to in the content.